

# Prediction of Control Effectiveness for a Highly Swept Unmanned Air Vehicle Configuration

Joe Coppin<sup>1</sup> and Trevor Birch<sup>2</sup>

*Defence Science and Technology Laboratory, Fareham, PO17 6AD, U.K.*

David Kennett<sup>3</sup>, George Hoholis<sup>4</sup> and Kenneth Badcock<sup>5</sup>

*University of Liverpool, Liverpool, L69 3GH, U.K.*

A study into the prediction of the effectiveness of different trailing edge controls on aUCAV configuration, on which complex vortical flow develops at moderate to high angles of attack, is described. Stability and control of these vehicles is demanding, and requires early knowledge of the changes in forces and moments from control surface deflections. Computational results are compared with data from wind tunnel tests over the Mach number range  $0.146 \leq M \leq 0.9$  for undeflected controls. The effectiveness of the controls at subsonic and transonic conditions is then discussed. The influence of the mesh treatment and turbulence model on the realism of the predictions is considered. The CFD predictions show good agreement with measurements, and show limited sensitivity to geometry treatment and turbulence model for the flow conditions where the controls are effective. CFD is shown to be capable of predicting the control surface influence, even at high speed.

---

<sup>1</sup> Aerodynamicist, Air and Weapons Systems Department, DSTL.

<sup>2</sup> Aerodynamics Fellow, Air and Weapons Systems Department, DSTL, Senior Member AIAA.

<sup>3</sup> Research Associate, CFD Laboratory, School of Engineering, University of Liverpool.

<sup>4</sup> PhD student, CFD Laboratory, School of Engineering, University of Liverpool.

<sup>5</sup> Professor, CFD Laboratory, School of Engineering, University of Liverpool.

## Nomenclature

$C_L$	= lift coefficient
$C_D$	= drag coefficient
$C_l$	= rolling moment coefficient (based on semispan)
$C_m$	= pitching moment coefficient (based on reference chord)
$C_n$	= yawing moment coefficient (based on semispan)
$C_p$	= pressure coefficient
$M_{(\infty)}$	= Mach number (free-stream)
$q_\infty$	= free-stream dynamic pressure (pa)
$p_t$	= total pressure (pa)
$p_{(\infty)}$	= free-stream static pressure (pa)
$Re$	= Reynolds number (based on reference chord)
$y^+$	= non-dimensional boundary layer parameter, $y^+ = yu_T/\nu$
$S_{ref}$	= reference area (planform area) ( $m^2$ )
$c_{ref}$	= reference chord (aerodynamic mean chord for high speed, root chord for low speed) (m)
$b_{ref}$	= reference span (semispan) (m)
$\alpha$	= angle of incidence (positive nose up)
$\nu$	= kinematic viscosity ( $m^2/s$ )

Acronyms:

CAD	Computer Aided Design
CFD	Computational Fluid Dynamics
DNW-NWB	German-Dutch Wind Tunnels - Low Speed Tunnel
DNW-TWG	German-Dutch Wind Tunnels - Transonic Wind Tunnel
DOF	Degrees Of Freedom
DSTL	Defence Science and Technology Laboratory
HPC	High Performance Computing
HSWT	High Speed Wind Tunnel (BAE-Systems Warton)
(L/R) IB	(Left/Right) Inboard (Flap)
(L/R) OB	(Left/Right) Outboard (Flap)
MPM	Model Positioning Mechanism
MRP	Moment Reference Point
MUSCL	Monotonic Upstream-centered Scheme for Conservation Laws
PMB	Parallel Multi-Block
RANS	Reynolds Averaged Navier-Stokes
SA	Spalart-Allmaras
SACCON	Stability And Control CONfiguration
UCAV	Unmanned Combat Air Vehicle

## I. Introduction

Key aerodynamic related issues for Unmanned Combat Aerial Vehicles (UCAV) relate to the generation of lift for take-off, and to controllability, especially in the absence of a vertical tail. The prediction of control surface effects then becomes critically important for the design of the vehicle. This can present a significant challenge for CFD as the control surfaces create additional geometrical and flow complexity, presenting demanding grid generation and turbulence modelling challenges.

There are a variety of options for representing control surfaces in CFD simulations, which can be split up into three types of methods. Firstly, the original geometry can be used, meshing the gaps between the flaps and the wing. When using a block-structured solver this leads to a significantly skewed mesh in those regions. Secondly, the geometry can be modified to include a blending region, allowing a simplified use of hexahedral blocks. These two methods were compared by Rampurawala [1], leading to the conclusion that this geometry simplification has minimal effect on the results for low angle of attack flutter and transonic buzz studies. Thirdly, overset grids have also been used successfully for flaps, rotorcraft and stores in bays [2–4], where overlapping grids allow a portion of the grid to be moved with the control surface.

An investigation into whether the gaps around the control surface in a wind tunnel model need to be taken into account for CFD simulations was conducted by Boelens for vortical flow on the X-31 aircraft [5]. This found that the predictions obtained for the behaviour of the integrated loads and flow topology were correct without having to resolve in detail the geometry around the gap correctly, despite the complex leading edge vortical flow that was present near the gaps.

The SACCON is a generic UCAV that has been used for Computational Fluid Dynamics (CFD) validation, aerodynamic studies in vortical flows and flight dynamics studies [6]. The configuration has a lambda wing planform, with a leading edge which causes interesting vortical flows. The leading edge is sharp close to the apex and the trailing edge, and has a relatively blunt profile in between. Apex and tip vortices are present at moderate angles of attack, and these interact and breakdown at high angles of attack [7]. The development and behaviour of these vortices provides a significant test for CFD, and many studies have been published on this topic [8–12].

This paper considers the prediction of the influence of trailing edge control surfaces for a UCAV.

Quantity	High speed	Low speed
Reference area ( $S_{ref}$ )	0.1173m <sup>2</sup>	0.77m <sup>2</sup>
Reference chord ( $c_{ref}$ )	0.23424m	0.479m
Reference span ( $b_{ref}$ )	0.3m	0.769m
MRP ( $x,y,z$ ) <sub>ref</sub> (from the nose)	(0.21204m, 0m, 0m)	(0.6m, 0m, 0m)

Table 1: Reference values for the SACCON wind tunnel tests.

A number of simulation options are considered, including the treatment of the geometry, and the turbulence model used. A detailed assessment of the ability to predict control surface forces and moments is made using experimental data. The paper starts with the test case description and of the simulation methods used. Then, the topology of the underlying flowfield is described. A detailed evaluation of results obtained at low speed is given, followed by a similar discussion for high speed results.

## II. Model Description

### A. Configuration

The SACCON configuration is a lambda wing UCAV with parallel leading and trailing edges. The design of the SACCON configuration is detailed in Reference [13]. The leading edge has a varying radius; sharp at the root and transitioning to round at the first crank and for the remainder of the wing. The root section is 12.5% thick so that the centre-body can house the intake, engine, and internal components; and the wing is 12% thick at the first crank, reducing to 7.3% at the second crank. The chord reduces to zero at the wingtip. There is also 5° of washout applied between the first and second cranks. Models of different size were used for wind tunnel tests at subsonic (labelled low speed) and transonic (labelled high speed) conditions, and their dimensions are given in Table 1.

### B. Controls

The SACCON wind tunnel model has cut-out trailing edges on the port and starboard sides to allow controls to be fitted. There is provision for two flaps on each wing between the first and

second cranks labelled IB (inboard) and OB (outboard), preceded by L or R to indicate the left or right side of the model as oriented in Fig. 1. For the high speed model the cut-out is approximately 20% of the local chord and the equivalent hinge line lies approximately at this location. For the low speed model the hinge line can be varied between 20% and 30% of the local chord, with the majority of the experiments conducted at 25%. In the inboard position, plain flaps, which can be deflected by  $0^\circ$  and  $\pm 10^\circ$ , can be fitted for the high speed model and deflections of  $0^\circ$ ,  $\pm 5^\circ$ ,  $\pm 10^\circ$  and  $\pm 20^\circ$  are possible for the low speed model. In the outboard position, plain flaps ( $0^\circ$  and  $\pm 10^\circ$  for the high speed and  $0^\circ$ ,  $\pm 5^\circ$ ,  $\pm 10^\circ$  and  $\pm 20^\circ$  for the low speed) or a split flap ( $\pm 5^\circ$ ,  $\pm 10^\circ$  or  $\pm 20^\circ$ ) can be fitted. These flaps, configured in various combinations, are intended to give pitch, roll and yaw control to the vehicle. Throughout the high speed wind tunnel test controls were primarily fitted to the port wing with some cases having controls on both sides to test for interference. For the CFD test cases, only port controls are deflected. The flaps are attached to the wing so that there is no gap present at the control root in the undeflected or deflected states.

### C. Experimental Overview

The high speed model was tested in the DNW-TWG [14, 15] wind tunnel in Göttingen Germany and in the BAE Systems HSWT in Lancashire, UK [14, 16]. For the high speed comparisons, only data from the HSWT are used. For the low speed model, data are used from the DNW-NWB wind tunnel in Braunschweig, Germany [17]. The BAE Systems HSWT is an intermittent blowdown tunnel with a 1.2 x 1.2m test section with run times of up to 30s. It can either be used in the transonic ( $0.4 < M < 1.14$ ) or supersonic ( $1.4 < M < 3.8$ ) regime, but for the SACCON test, Mach numbers in the range  $0.5 < M < 0.9$  were tested. The DNW-NWB wind tunnel is a closed circuit low speed wind tunnel of atmospheric type with a 3.25 x 2.8m test section. It can operate at Mach numbers up to 0.27, with a Mach number of approximately 0.146 for the experimental data used in this paper. For the high speed tests boundary layer transition was fixed in the experiment using the “Boeing Dot” method [16]. The dots were supplied using pre punched adhesive tape and placed 3.2mm behind the leading edge on the upper and lower surfaces. The dot height was  $183\mu\text{m}$ , the diameter was approximately 1.25mm and the dots were placed 1.25mm apart. The majority of runs

had transition fixed in this way but some runs were completed with free transition. For the low speed tests a removable latex based paint was used to fix the transition [17]. In the HSWT experiment, the reservoir total pressure was nominally set to 138Kpa and the desired Mach number was set using the 2nd throat. There is also a Mach flap system in the tunnel to compensate for model blockage. Total pressure ( $p_t$ ), dynamic pressure ( $q_\infty$ ) and Reynolds number ( $Re$ ) were recorded for each point. Run averaged values were used to derive the free-stream conditions for the CFD calculations. The free-stream conditions for the undeflected clean configuration at zero sideslip were used for all of the corresponding CFD calculations to provide consistency. The high speed model was mounted on a six component internal balance connected to a rear sting. The test comprised mainly of force and moment runs at fixed Mach numbers in continuous sweep mode, where the model incidence was varied. Some data was also acquired in pitch pause mode, where model incidence was fixed. The low speed model was suspended by a belly sting from a 6-DOF platform MPM [17]. Force and moment data and surface pressures at four slices along the wing were collected. The location of the slices can be seen in Fig. 1.

### III. Formulation

#### A. Geometry and CAD

The geometry used for the CFD calculations is based on the high speed wind tunnel model geometry which was defined by as a number of CAD parts. The CAD file contained the baseline configuration with cut-outs for the control surfaces and a truncated sting. This file was modified in two ways; the sting was truncated with a tangent ogive rather than a hemisphere to reduce numerical problems, and the gaps around the edges of the control surfaces and wing cut-outs were filled to avoid holes in the geometry when the control surfaces were deflected. Separate CAD files for each control surface at each deflection angle were extracted from the original files, IB, and OB flaps at  $0^\circ$  and  $\pm 10^\circ$ . The split flap geometry was produced by importing the OB flaps at  $\pm 10^\circ$  as no CAD was available, see Fig. 2(b). There was no need to intersect components or remove internal surfaces as this was not required by the mesh generator.

## B. Mesh Generation

Two different mesh generators were used for the unstructured solver in this study. First for the clean aircraft, ICEM TETRA and PRISM were used to generate a predominantly tetrahedral mesh with prism layers to resolve the boundary layer. The farfield was placed  $>20$  semi-spans from the UCAV and the 1st cell height was set to give a  $y^+$  of  $O(1)$ . The resulting mesh size was 14 million cells for the full aircraft, Fig. 3(a).

The second set of meshes (example in Fig. 3(b)) was used to investigate the incremental forces and moments from control deflections. These were generated using BOXERMesh, which enables meshing around complex configurations with minimal effort spent manipulating CAD. These meshes comprised predominantly of hexahedral cells with prism layers near the walls. The mesh generator was scripted so that meshes could be automatically generated and each configuration was successfully meshed without user intervention. These meshes are all half models (symmetry) and are relatively large compared with the ICEM meshes with similar surface spacing. This is mainly because the mesh is not permitted to grow away from the surface as quickly as is possible for tetrahedral meshes. Furthermore, a finer surface mesh is also required to accurately capture the geometry. The half mesh size for each configuration was approximately 23 million cells. To assess the grid sensitivity, coarse (8.8 million) and fine (64 million) meshes were also generated. This was done by scaling the farfield mesh size, which controls all other mesh spacings and approximates to isotropic refinement apart from in the normal direction in the prism layer region. For the intermediate mesh the first cell height was larger than ideal for low  $y^+$  wall treatment (average  $y^+=5.9$ ). This is due to a cell aspect ratio limit in BOXERMesh. To overcome this a very fine surface mesh would be required which would result in prohibitively large mesh sizes. The average  $y^+$  for the fine mesh was approximately 3.

The block structured grids that were generated all come from one parent grid from which the others were built. The parent grid is for the high speed model with no control surface deflections, and is a structured multi-block grid, generated using the grid generation software ANSYS ICEM. The grid consists of approximately 17 million points and 16 million cells; with 260 blocks in total. Initial cell sizes and number of cells in each direction were based on a grid used for earlier work [18], which included a grid convergence study. The basic block topology of the grid and the distribution

on the upper surface can be seen in Fig. 3(c). There is a C-blocking around the leading edge, an O-grid at the blunt tip and a H-grid around the trailing edge. The first cell spacing normal to the solid wall is around  $1 \times 10^{-5} c_{ref}$ , for the low speed, and  $1 \times 10^{-6} c_{ref}$ , for the high speed, ensuring a  $y^+ \leq 1$ . The full body is simulated for all block structured results.

Work was done by Rampurawala [1] on the treatment of control surfaces with structured multi-block solvers. This work investigated two of the options available: first, leaving the flap geometry as it is, and blocking the gap between the flap and the wing; second, using a blending region between the wing and the flap to go from the trailing edge geometry of the wing to the flap geometry in a smooth fashion. In this work the second option is used, as the first one results in low quality cells in the gap due to the skewness, increases the refinement required significantly and also results in a much poorer convergence rate. Blocking the gap would also require the generation of a new grid for each flap configuration.

The flap geometry is known for the SACCON, so the blending process was done during the grid construction stage, instead of within the solver as is done in Ref. [1] for aeroelastic applications. This was done by cutting the surface geometry, at either end of the flap, and using this as a blending region. Surfaces were then constructed within this region to obtain continuity between the wing and the flap in the spanwise direction, Fig. 4. The blocking generated for the original grid, can then be loaded onto this new geometry, and the block faces reassociated so that the original grid connectivity is maintained.

### C. Flow Solver

Computations were carried out by DSTL using the commercially available unstructured Navier-Stokes flow solver Cobalt [19] v6.1. Cobalt employs a cell centred finite volume discretisation and a Godunov exact Riemann solver with least squares reconstruction to provide second-order accuracy. A variety of turbulence models are available in Cobalt although all of the results presented in this paper were obtained using the standard Spalart-Allmaras model [20].

The majority of CFD calculations were run assuming fully turbulent flow. Some additional CFD runs were completed using the Spalart-Allmaras model with a trip term [20] in order to simulate

the transition fixing used in the wind tunnel test. In this case, strips of cells on the upper and lower surfaces were marked as trip cells in the region  $0.014\% c_{ref} < x < 0.026\% c_{ref}$ . For the SA model with trip term, the free-stream eddy kinematic viscosity is  $\nu = 0.1\nu_{mol}$  compared with  $\nu = 3.0\nu_{mol}$  for the standard SA model. Computations were run on the DSTL HPC cluster using 600 cores for 800 iterations each. No convergence problems were encountered and the forces and moments were typically converged to steady state in fewer than 500 iterations. Residual convergence was also checked and the continuity equation residual typically reduced by over 6 orders.

The unstructured CFD calculations with deflected controls were completed on half body meshes for the port wing only. In order to obtain force and moment coefficients for the complete configuration to compare with the wind tunnel results, loads from the clean starboard wing were required before computing the coefficients. These were obtained from a clean port wing calculation which was then mirrored. This assumes that the flow on the port and starboard wings are independent. Using half meshes (assuming symmetry) significantly reduces the mesh size and hence computational time to just over half of that required for a full wing. Control increments for roll, pitch and yaw were calculated by subtracting the force and moment coefficients of the undeflected configuration from the coefficients of the configuration of interest.

The flow solver used at the University of Liverpool is a research code called parallel multi-block (PMB) [21]. PMB uses a cell-centred method on block-structured meshes; these blocks are spread across processors for parallel computations. In this work PMB solves the Reynolds-Averaged Navier-Stokes (RANS) equations with Osher's Riemann solver, MUSCL upwinding and a slightly modified  $k-\omega$  turbulence model. The modification to the original model is a source term modification introduced by Brandsma et al. [22], which reduces the amount of turbulent kinetic energy produced within the vortex core.

The mean and turbulence equations are solved decoupled in an implicit manner, with approximate Jacobian matrices based on the first order sparsity pattern, and a Krylov subspace iterative solver. The grids used in this work have a far-field that is 20 times the reference chord length away from the geometry. Ghost cells are used for the solid wall boundary conditions - there are two adjacent to the wall. The solutions were judged to be converged when the residual had been

reduced by six orders of magnitude.

#### IV. No Control Surface Deflections: Flow Topology

The SACCON exhibits complicated flow regimes that cause nonlinearities in the force and moment coefficients as the angles of attack, sideslip and roll are varied. The case at a Mach number of 0.146 is used to illustrate the baseline flow; and as the pitching moment coefficient is most sensitive to changes in the flow topology, it is used to illustrate the different flow regimes as the angle of attack is increased, see Fig. 5(a). The description here follows that of Ref. [7].

At low angles of attack the pitching moment changes linearly with angle of attack, with attached flow over the wing. This flow arrangement persists until around 10 degrees angle of attack (Fig. 5(b)) when a vortex forms at the wing tip, where the wing profile is sharp. As the angle of attack increases to 15 degrees, an apex vortex has formed, which tracks the sharp leading edge, and then moves inboard. Meanwhile, the tip vortex onset location continues to move forward (see Fig. 5(b)). During this angle of attack range the moment continues to increase, but now is below the linear trend. By around 15 degrees angle of attack the onset of the tip vortex has reached the section on the wing where the profile is blunt. The motion of the tip vortex continues forward with increasing angle of attack, illustrated in Fig. 5(c) at 17 degrees. The pitching moment reduces because of the forward motion of the tip vortex, until there is no attached flow between the apex vortex and the tip vortex, at which angle of attack the pitching moment coefficient stops decreasing. Then the apex and tip vortices interact, and this combined region of vortical flow has a vortex breakdown location which moves forward with increasing angle of attack, causing an increasing pitching moment. The flow pattern therefore consists of two vortices, whose onset locations change in a nonlinear fashion with the angle of attack, and which eventually interact and breakdown.

A similar flow topology is seen at higher Mach numbers, with the exception of  $M=0.9$  which will be discussed shortly. The vortical flow features remain the same, with the forward motion of the tip vortex and the vortex breakdown occurring at lower angle of attacks as the Mach number is increased. This can be seen in the pitching moment coefficient curves, see Fig. 6, as the dip occurs at a lower angle. At a Mach number of 0.9 a shock has formed on the upper surface. The effect of

Experiment	$M_\infty$	$Re [\times 10^6]$	LOB [ $^\circ$ ]	LIB [ $^\circ$ ]	ROB [ $^\circ$ ]	RIB [ $^\circ$ ]	$\alpha$ [ $^\circ$ ]
RN1007	0.146	1.57	0	0	0	0	10
RN1008	0.146	1.57	0	0	0	0	15
RN1092	0.146	1.57	0	-20	+20	0	10, 15
RN1114	0.146	1.57	-20	0	0	+20	10, 15
RN1103	0.146	1.57	-20	-20	+20	+20	10, 15

Table 2: Summary of low speed cases performed.

this on the skin friction streamlines and the flow around the trailing edge can be seen in Fig. 6(d).

## V. Low Speed Results

### A. Clean Configuration

Table 2 contains a summary of the low speed results presented here, which are from the block structured code. The results from run 1007 and 1008 are first considered to validate the predictions of cases with no flap deflections. A comparison of the surface pressure coefficients with measurements is shown in Fig. 7. At an angle of attack of  $10^\circ$ , Fig. 7(a), the surface pressures are predicted well for all the slices. As expected from the description above, no well developed vortices are present. At the higher angle of  $15^\circ$ , Fig. 7(b), discrepancies with the experimental data are visible in the regions dominated by the vortices. The track of the apex vortex appears to be mislocated through the 45% slice, although the measurements are too sparse to evaluate this in detail. The onset of the tip vortex has not reached the 89% slice in the computation, whereas the flat region in the measurements indicates that this has happened in the experiment. At this angle of attack there is also minor asymmetry in the measurements which arises from some unsteadiness in the flow. Overall, the comparison indicates good agreement between the computed and measured results.

The effect that the choice of turbulence model has on the surface pressure coefficients is also shown in Fig. 7(b). One equation, two equation and a modified two equation model for vortical flow are used. At the low angle of attack there is no visible difference in the results between the different turbulence models. As the strength of the vortices increases we start to see minor differences appearing. There is a slight difference in the location and strength of the apex vortex

passing through the slice at 45%. There is also a difference in the suction levels at the leading edge at the slice at 89%, perhaps indicating a difference in the tip vortex onset location. However, there is only a very minor influence of the turbulence model in this angle of attack range, which is used for the cases with control surfaces deflected.

At higher angles of attack, more significant differences appear between different turbulence models. There are vortex substructures in the shear layer, which RANS calculations are generally not able to resolve [11]. There is also difficulty in predicting the separation along the rounded leading edge, which occurs at this higher angle of attack range; and the separation line is especially sensitive to the turbulence model used [11, 12]. Unsteady flow phenomena associated with leading edge vortices, such as vortex breakdown, become significant at higher angles of attack and are not predicted. These effects are all beyond the scope of the paper.

## **B. With Controls deflected**

Control surface deflections are represented in the block structured code by a mesh deformation, as described in Section III B. An additional case was used first to test the effect of the width of the blending region used. For this, three geometries were used for the left outboard  $+20^\circ$ , left inboard  $+20^\circ$  configuration. The blending region across the deformation has lengths 15% (narrow), 25% (medium) and 35% (wide) of the flap chord, Fig. 8(b). The pressure coefficient at various slices along the wing and the convergence histories are given in Figs. 8(a) and 8(c), at angles of attack  $10^\circ$  and  $15^\circ$ , respectively. From these plots we can see that there is no difference between the pressure distributions arising from the blending gradients, and the difference in convergence rates, Fig. 8(d), is negligible, indicating that the influence of the detailed geometry around the flap has little impact on the apex and tip vortices that dominate the flow. It should be noted, however, that the narrow blending can sometimes create negative cell volumes around the flap for certain deflections requiring additional adjustments to the mesh; as a result the medium blending of 25% of the flap chord is used for the remainder of the calculations in this work. Pressure distribution cuts across the blended flap are shown in Fig. 8(e), for the slice indicated in Fig. 8(f). The differences in the blending region are clear, as would be expected, but on the main body of the flap there is virtually no difference in

pressure levels.

The low speed, static calculations with deflected flaps, listed in Table 2, were performed at  $M_\infty = 0.146$ ,  $Re = 1.5709 \times 10^6$ , at angles of attack  $10^\circ$  and  $15^\circ$ . The increments in the pitching and rolling moment coefficients are presented in Figs. 9(a) and 9(b), respectively. In this figure, the experimental data is shown with lines, and computations, at the two angles of attack, with symbols. The increments between the undeflected case and the three combinations of flap deflections are similar. The measured and computed values of the pitching moment have a similar offset for all cases. This has been shown to be down to not representing the belly mounted sting in the computation and using RANS models [12]. The rolling moment values are in good agreement with measurements.

The pressure coefficients are shown, with the experimental data, for each of the test cases at  $\alpha = 10^\circ$  and  $\alpha = 15^\circ$  in Figs. 10 and 11, respectively. The comparisons are very similar to those with no flap deflections, explaining why the pitching moment comparisons are similar for the combinations of deflected flaps. Deflecting the flap up on one side tends to delay the formation of the tip vortex in the experiments, and there is a suggestion in the computed results at the 89% slice that the onset is being promoted when the flap is deflected down, indicated by the inboard location of the suction peak.

The flap deflections tend only to influence the details of the tip vortex, and the experimental data is not refined enough to allow these influences to be examined in detail. The increments in the pitching and rolling moments are nonetheless well predicted by the computations.

## VI. High Speed Results

### A. Clean Configuration

Force and moment measured data are available, but no surface pressures, to validate the high speed case predictions. Table 3 contains a summary of the high speed cases presented here with results obtained from both the unstructured and structured codes. Fig. 12 shows the lift, drag and pitching moment comparisons for the clean configuration at Mach numbers of 0.5, 0.7 and 0.9. Two sets of experimental data are presented, one transition free and one transition fixed. For each Mach

Experiment	$M_\infty$	Re [ $\times 10^6$ ]	configuration	$\alpha$ [°]
R264-0059	0.5	14.35	clean	0-20
R264-0047	0.7	18.81	clean	0-20
R264-0058	0.9	20.68	clean	0-20
R264-0078	0.7	18.81	inboard $+10^\circ$	0-20
R264-0071	0.7	18.81	inboard $-10^\circ$	0-20
R264-0099	0.7	18.81	outboard $+10^\circ$	0-20
R264-0104	0.7	18.81	outboard $-10^\circ$	0-20
R264-0092	0.7	18.81	split $\pm 10^\circ$	0-20
R264-0140	0.7	18.81	inboard $+10^\circ$ , outboard $-10^\circ$	0-20
R264-0127	0.7	18.81	inboard $-10^\circ$ , outboard $+10^\circ$	0-20

Table 3: Summary of high speed cases performed.

number, lift is accurately predicted up to flow breakdown, when abrupt changes in pitching moment are also seen.

At  $M_\infty=0.5$ , some nonlinear vortex lift is evident between  $13^\circ < \alpha < 16^\circ$ , indicated by a steepening of the lift curve slope. This phenomenon is not evident at  $M \geq 0.7$ . At all Mach numbers, the incidence at which the wing stalls is over estimated by the CFD, occurring approximately  $2^\circ$  later than indicated in the experiment. In each case the zero lift drag is over predicted by approximately  $\Delta C_D \approx 0.0025-0.003$  accounting for around 30% of the total drag compared with the transition fixed result. There is also a significant difference between the experimental data for transition fixed and transition free. At incidences above  $\alpha=12^\circ$  the drag predicted by the CFD is generally closer to that measured in the wind tunnel. For the pitching moment the CFD results diverge from the experiment with increasing Mach number. The measured pitching moment characteristics are nonlinear and some significant differences are evident between the transition fixed and free measurements. The predictions are typically more linear than the measured data until just before the pitchup, which is generally predicted to occur at a higher incidence.

At  $M=0.5$ , development of the vortical flow with increasing angle of attack is very similar to the low speed case described above. The surface pressure distribution at  $10^\circ$  and  $14^\circ$  angle of attack

is shown in Fig. 13 and shows the trailing edge vortex footprint at the lower angle, and the trace of the apex vortex at the higher angle.

The flow development at  $M=0.7$  (Figs. 13(c) and 13(d)) is largely similar to that at  $M=0.5$  although some effects due to compressibility can be seen. Shock footprints parallel to the leading edges are visible at  $\alpha=10^\circ$ , although these do not seem to alter the surface flow pattern much. At  $\alpha=14^\circ$  the apex separation is slightly larger than at  $M=0.5$  and the tip vortex is less concentrated, increasing in diameter more quickly and providing less additional vortex lift. It is unclear as to whether this is caused by shock interactions or just the increased pressures caused by compressibility. This trend continues at the higher incidence angles.

At  $M=0.9$  (Figs. 13(e) and 13(f)), the wing flow becomes quite different. There is a strong lambda shock, of which the trailing leg extends inboard all the way to the root, forming an arc on the upper surface joining the wingtips and the first trailing edge cranks. This trailing shock causes almost all of the trailing edge flow to be separated even at low incidence angles. Additionally the leading part of the lambda shock causes kinks in the surface flow streamlines when  $\alpha \leq 10^\circ$  and flow separation at  $\alpha=12^\circ$  and above. These shock separations replace the leading edge separation seen at the lower Mach numbers and they occur at a lower incidence.

## **B. With Controls deflected**

Several cases with control surfaces deflected were computed. The unstructured results use a conforming mesh around the deflected configuration, including all gaps and surfaces, as described in section III. Block structured results were obtained using the blending approach used for the low speed results. The unstructured results used the Spalart-Allmaras turbulence model, whereas the block structured results used the  $k - \omega$  model with a rotation correction.

First, outboard and inboard flap deflections are considered. The incremental forces and moments are shown in Fig. 14 at a Mach number of 0.7, for  $\alpha$  between  $0^\circ$  and  $20^\circ$ . Until  $10^\circ$  there is generally a close agreement between the two sets of CFD predictions and the measurements. After this, there is more scatter, but still the measurements and computations are in reasonable accord.

At low incidence the deflected flaps behave in the correct sense in the pitch and roll axes and

both deflections provide approximately the same control effectiveness. The control effectiveness is reasonably well predicted in all three axes. As the incidence is increased a positive deflection (trailing edge down) becomes more effective (in the pitch and roll axes), whereas the negative deflection (trailing edge up) becomes less effective. This is because for the negative deflection, the flap enters the wake of the wing and experiences a lower dynamic pressure; whereas for the positive deflection, the flap is pushed out into the relatively undisturbed air. In the yaw axis, the positively deflected control creates a positive moment (nose to starboard) and a negative deflection creates a negative moment. These moments are in the wrong sense for the usual arguments to be correct about adverse yaw being caused by increased profile or induced drag. The reasons for these yawing moments are not known. Flow visualisation shows that the flow readily separates on the upper surface of the positively deflected flap, even at  $\alpha=0^\circ$ . As incidence increases, the boundary layer approaching the flap has less momentum, and the separated region becomes larger and reverse flow is seen. Negative deflections help to encourage the upper surface flow near the trailing edge to stay attached until higher incidence angles. At high incidence angles the flap experiences reverse flow from an upstream separation although the vortex flow is fairly weak by the time it reaches the OB flap. On the lower surface, the flow stays attached across the incidence range, even for negative deflections where an adverse pressure gradient is seen.

For the inboard flap, the trends are similar to the outboard flap at low incidences. The agreement between the numerical predictions and experimental measurements is generally not as good as for the OB flap. Rolling moment increments are over predicted for both deflections, and pitching moment increments are over predicted for the negative deflection. At higher angles of attack ( $15^\circ \leq \alpha \leq 20^\circ$ ), in the roll and pitch axes, a reduction in control effectiveness is observed in the experiment and predicted numerically. In the yaw axis, at low incidence the moment increments are in the same sense to those of the outboard flap. The moment increments increase in magnitude with increasing incidence before a strong reversal is seen at  $\alpha=15^\circ$ . This reversal is also seen in the experiment, but is stronger in the numerical result. At  $\alpha=20^\circ$  the control is still reversed but the magnitude of the force has reduced. The flow visualisation (Fig. 15) shows similar effects to those seen for the OB flap although now the upper surface boundary layers seem to separate more readily. This

is thought to be because the incoming boundary layer has travelled further and there has been an upstream separation caused by the sharp leading edge at the apex. For negative deflections, on the lower surface of the flap, the flow stays attached across most of the incidence range, although at  $\alpha=15^\circ$  there is some spanwise flow visible (Fig. 15(f)). At high incidence, when the tip and apex vortices begin to combine, the flap is quite close to a strong vortex flow. This is thought to be responsible for the control reversal and large yawing moment increments observed, although the exact mechanism is not known and requires further investigation.

The surface pressure distributions at  $10^\circ$  angle of attack are shown in Fig. 16. The unstructured and block structured results are in good agreement, except in the region around the blending, showing the limited influence of the turbulence model and grid treatment for this case.

Next, cases with the split and crow flaps were considered using the unstructured code. Comparisons between the predictions and measurements are shown in Fig. 17 and in general both sets of data are in good agreement.

The split flap is used primarily for yaw control. This was not simulated by the block structured solver as it creates significant challenges for the multi-block grid generation. Fig. 17(c) shows that for  $\alpha < 7.5^\circ$ , the control deflection acts in the correct sense; developing additional drag and turning the nose in the direction of the control being deployed. The magnitude of the yawing moment being generated is only marginally more than for the plain OB flap when it is negatively deflected. At higher angle of attack, a control reversal is seen before a return to the correct sense at  $\alpha=15^\circ$ . In the roll and yaw axes, the moments generated are initially small at low incidence and increase with increasing incidence. The direction of the moment increments is consistent with a loss in lift on the wing with the control surface deployed. The unstructured results predict these trends reasonably within the resolution of the data points.

Crow flaps are also primarily intended to be used as yaw controls by generating additional drag forces. Fig. 17(f) shows that the crow flaps are only effective in the correct sense for  $\alpha < 10^\circ$ , although for OB +10/IB -10 the force that is generated is very small. Above  $\alpha=10^\circ$ , OB -10/IB +10 operates in the wrong sense throughout the rest of the range whereas OB +10/IB -10 returns to be in the correct sense. These moments are clearly driven by the large IB flap forces discussed

above. Again, similar to what was seen with the split flap, both configurations generate pitch and roll moments consistent with a loss in lift on the port wing. The agreement for pitch and roll between the numerical result and the experiment is reasonable here. The flow visualisation in Fig. 18 shows that the surface flow patterns are very similar to those for the individual deflections. The only noticeable differences are in a small region on the OB flap where the wake (a small vortex) from the edge of the upstream flap can be seen. This is thought to have minimal effects on the forces and moments.

## VII. Conclusions

This paper has reported a study into the prediction and interpretation of control surface effects on the SACCON UCAV model at low and high speeds. Two CFD codes were used, with different geometric treatments of the flap. Limited sensitivity to the blending treatment, or to an exact geometric representation, was observed. The structured approach is simpler and more efficient in terms of the computational power needed, however, it is not suitable for simulating controls which effect the topology of the mesh. In contrast to this, the unstructured approach requires much less work during the grid generation process and can handle a larger variety of controls. The flow predictions were not found to be sensitive to the turbulence modelling used. Control increments were well predicted, in accord with measurements. This was the case despite the complexity of the underlying flow for the undeflected case. The study has demonstrated that CFD can provide useable data for control studies, with or without elaborate mesh treatments.

## Acknowledgments

The work reported here was undertaken as part of a NATO Science and Technology Organisation collaborative activity. The authors would like to thank Martin Rein from DLR, who provided the wind tunnel model and Glyn Rigby from BAE-Systems who lead the wind tunnel test. This research has been supported by BAE SYSTEMS and the Technology Strategy Board as part of the Simulation at Off-Design Conditions (SimOD) group. Special thanks is also extended to the AVT-201 team members for their efforts in obtaining CFD and experimental data, and also for their subsequent discussions and advice.

## References

- [1] Rampurawala, A. M. and Badcock, K. J., “Evaluation of a Simplified Grid Treatment for Oscillating Trailing-Edge Control Surfaces,” *Journal of aircraft*, Vol. 44, No. 4, 2007, pp. 1177–1188.
- [2] Steger, J. L. and Benek, J. A., “On the use of Composite Grid Schemes in Computational Aerodynamics,” *Computer Methods in Applied Mechanics and Engineering*, Vol. 64, No. 1, 1987, pp. 301–320.
- [3] Meakin, R. L. and Suhs, N. E., “Unsteady Aerodynamic Simulation of Multiple Bodies in Relative Motion,” *AIAA paper*, Vol. 1996, 1989, p. 1989.
- [4] Van Dam, C. P., Chow, R., Zayas, J. R., and Berg, D. E., “Computational Investigations of Small Deploying Tabs and Flaps for Aerodynamic Load Control,” in “Journal of Physics: Conference Series,” IOP Publishing, Vol. 75, August, 2007, p. 012027.
- [5] Boelens, O. J., “CFD Analysis of the Flow Around the X-31 Aircraft at High Angle of Attack,” *Aerospace Science and Technology*, Vol. 20, No. 1, 2012, pp. 38–51.
- [6] Loeser, T. D., Vicroy, D. D., and Schütte, A., “SACCON Static Wind Tunnel Tests at DNW-NWB and 14’x22’ NASA LaRC,” in “28th AIAA Applied Aerodynamics Conference,” , 2010.
- [7] Schütte, A., Hummel, D., and Hitzel, S. M., “Numerical and Experimental Analyses of the Vortical Flow Around the SACCON Configuration,” in “28th AIAA Applied Aerodynamics Conference,” , 2010.
- [8] Schütte, A., Huber, K., and Boelens, O., “Static and Dynamic Numerical Simulations of a Generic UCAV Configuration with and without Control Devices,” in “32nd AIAA Applied Aerodynamics Conference,” , 2014.
- [9] Zimper, D. and Rein, M., “Experimental and Numerical Analysis of the Transonic Vortical Flow Over a Generic Lambda Wing Configuration,” in “32nd AIAA Applied Aerodynamics Conference,” , 2014.
- [10] A., J., Cummings, R. M., Schütte, A., and Huber, K., “The NATO STO AVT-201 Task Group on Extended Assessment of Stability and Control Prediction Methods for NATO Air Vehicles: Summary, Conclusions and Lessons Learnt,” in “32nd AIAA Applied Aerodynamics Conference,” , 2014.
- [11] Tormalm, M. and Schmidt, S., “Computational Study of Static and Dynamic Vortical Flow Over the Delta Wing SACCON Configuration Using the FOI Flow Solver Edge,” in “28th AIAA Applied Aerodynamics Conference,” , 2010.
- [12] Cummings, R. M. and Schütte, A., “Integrated Computational/Experimental Approach to Unmanned Combat Air Vehicle Stability and Control Estimation,” *Journal of Aircraft*, Vol. 49, No. 6, 2012, pp. 1542–1557.
- [13] Hitzel, S., “Stability and Control Configuration - Aerodynamic Layout for Test Wing,” *RTO-AVT-161 Internal document*.

- [14] Rein, M., Irving, J. P., Rigby, G., and Birch, T. J., “High speed static experimental investigations to estimate control device effectiveness and S&C capabilities,” in “32nd AIAA Applied Aerodynamics Conference,” , 2014.
- [15] Rein, M., “Measurements of Aerodynamic Forces and Moments on the DLR F17E Model in Low- and High-Speed Flows,” *DLR Report No. IB 224-2011*.
- [16] Fairhurst, D. J., “A Summary of SACCON DLR-F17E Tests Carried out on Model RA234 in the Warton 1.2m High Speed Wind Tunnel,” *BAE-WEIS-RP-ASF-WTD-119741 WP070-O-005*, BAE Systems, Warton, United Kingdom.
- [17] Huber, K. C., Vicroy, D. D., Schütte, A., and Hübner, A. R., “UCAV Model Design and Static Experimental Investigations to Estimate Control Device Effectiveness and Stability and Control Capabilities,” in “32nd AIAA Applied Aerodynamics Conference,” , 2014.
- [18] Vallespin, D., Da Ronch, A., Badcock, K. J., and Boelens, O., “Vortical Flow Prediction Validation for an Unmanned Combat Air Vehicle Model,” *Journal of Aircraft*, Vol. 48, No. 6, 2011, pp. 1948–1959.
- [19] Grismer, M. J., Strang, W. Z., Tomaro, R. F., and Witzeman, F. C., “Cobalt: A Parallel, Implicit, Unstructured Euler/Navier–Stokes Solver,” *Advances in Engineering Software*, Vol. 29, No. 3, 1998, pp. 365–373.
- [20] Spalart, P. R. and Allmaras, S. R., “A One-Equation Turbulence Model for Aerodynamic Flows,” .
- [21] Badcock, K. J., Richards, B. E., and Woodgate, M. A., “Elements of Computational Fluid Dynamics on Block Structured Grids Using Implicit Solvers,” *Progress in Aerospace Sciences*, Vol. 36, No. 5, 2000, pp. 351–392.
- [22] Brandsma, F. J., Elsenaar, A., and Kok, J. C., “Leading Edge Vortex Flow Computations and Comparisons with DNW-HST Wind Tunnel Data,” in “NATO Research and Technology Organization Neuilly-Sur-Seine (France), Proceedings of the RTO/AVT Vortex Flow Symposium, Loen, Norway, 7-11 May, 2001,” , 2003.
- [23] Vallespin, D., Badcock, K. J., Da Ronch, A., White, M. D., Perfect, P., and Ghoreyshi, M., “Computational Fluid Dynamics Framework for Aerodynamic Model Assessment,” *Progress in Aerospace Sciences*, Vol. 52, 2012, pp. 2–18.

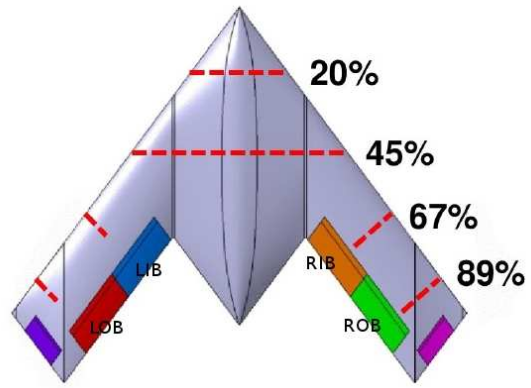
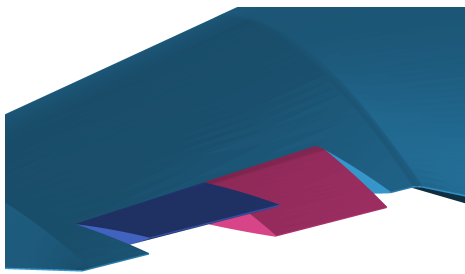
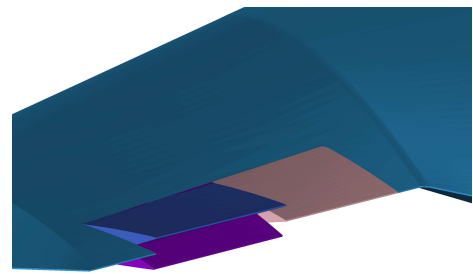


Fig. 1: Location of slices in the experiment.

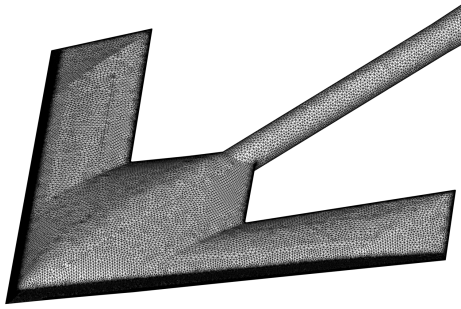


(a) Crow flap.

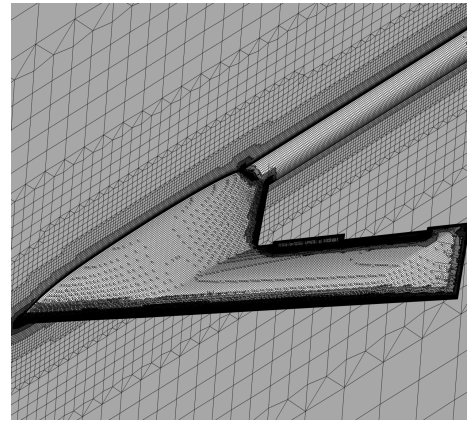


(b) Split flap.

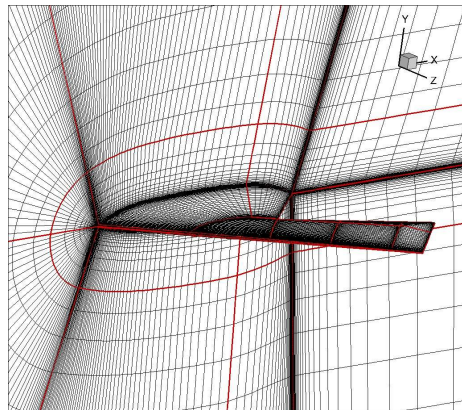
Fig. 2: Crow and split flap geometries.



(a) Unstructured ICEM grid for clean configuration.



(b) BOXERMesh grid for crou flaps.



(c) Structured grid.

Fig. 3: Topology for the grids used for the CFD simulations.

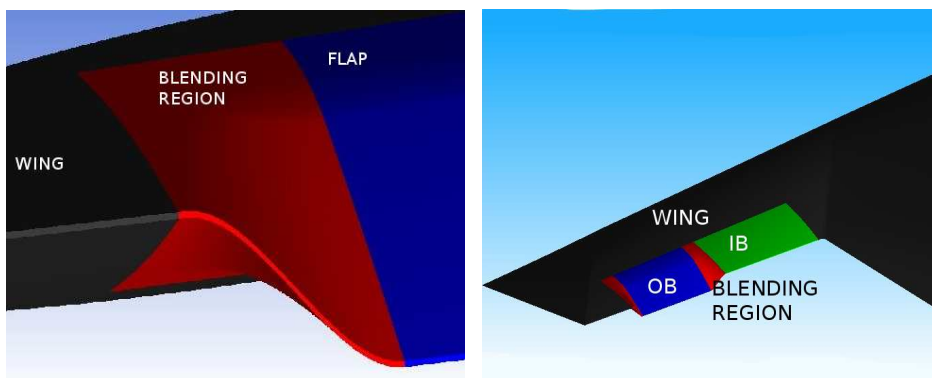
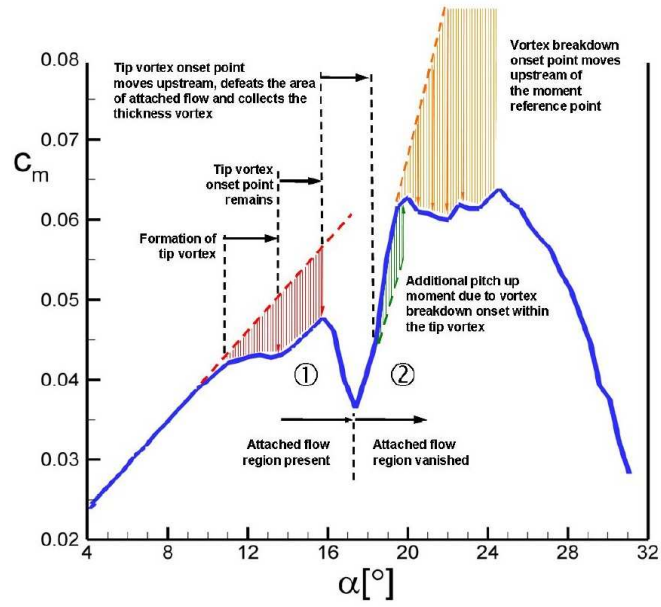
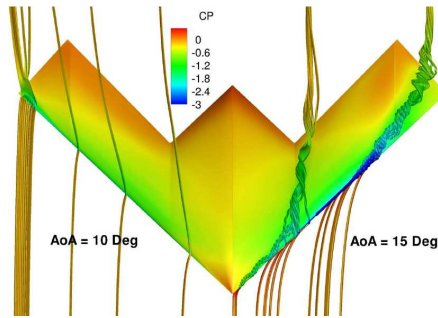


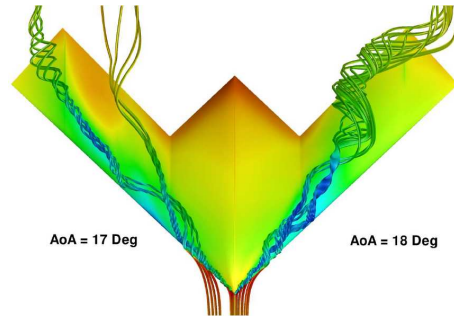
Fig. 4: Screenshot of the region between the wing and flap used as a blending region.



(a) Pitching moment coefficient (from Ref.[7]).

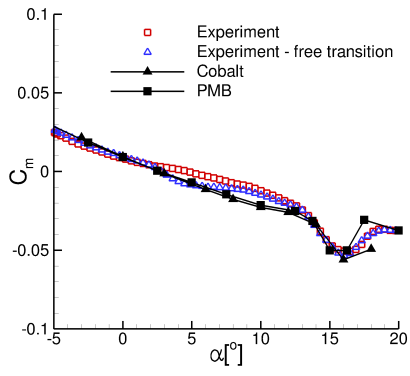


(b) Flow visualisation (from Ref.[23]).

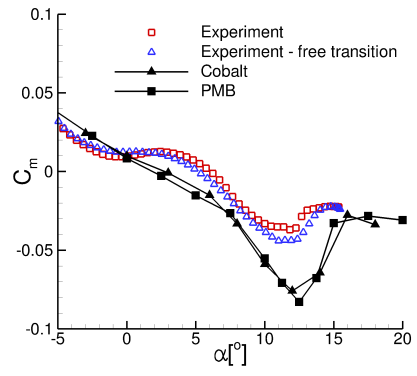


(c) Flow visualisation (from Ref.[23]).

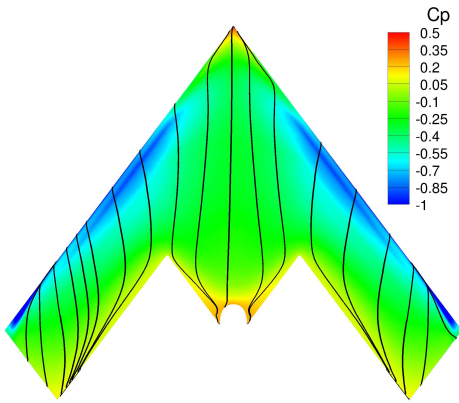
Fig. 5: Pitching moment coefficient as function of  $\alpha$  with an interpretation of how the vortex flow topology is affecting the aerodynamic behavior. Flow visualisation for the clean configuration at  $M=0.146$ .



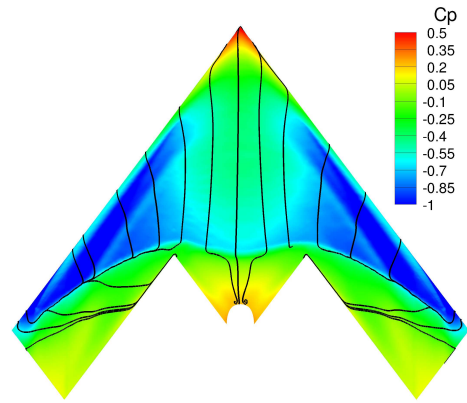
(a)  $M=0.5$ .



(b)  $M=0.9$ .

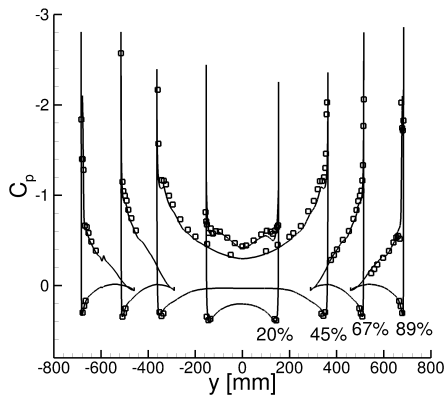


(c)  $\alpha=8^\circ$ ,  $M=0.5$ .

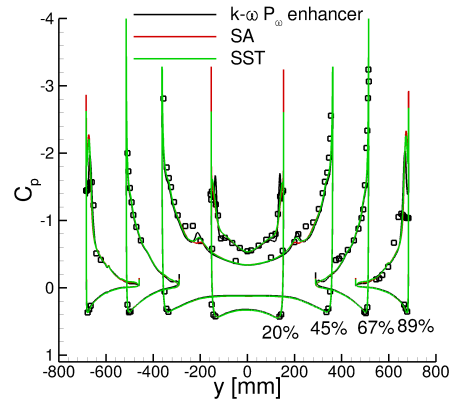


(d)  $\alpha=8^\circ$ ,  $M=0.9$ .

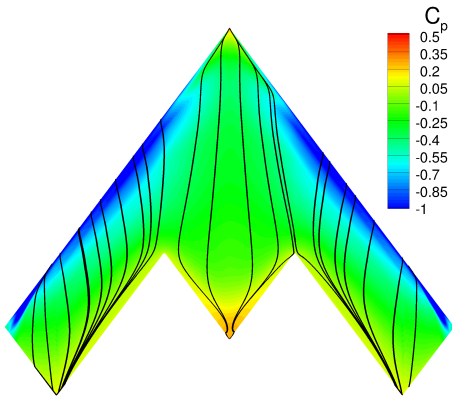
Fig. 6: Pitching moment coefficient and flow visualisation for the clean configuration at two Mach numbers,  $C_p$  contours and skin friction streamlines, unstructured results.



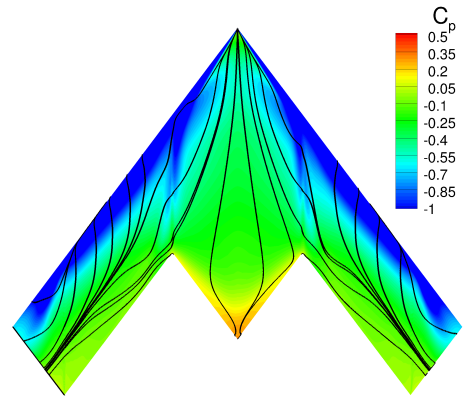
(a)  $\alpha=10^\circ$ .



(b)  $\alpha=15^\circ$ .

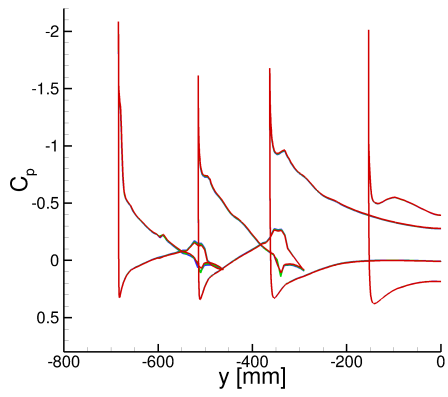


(c)  $\alpha=10^\circ$ .

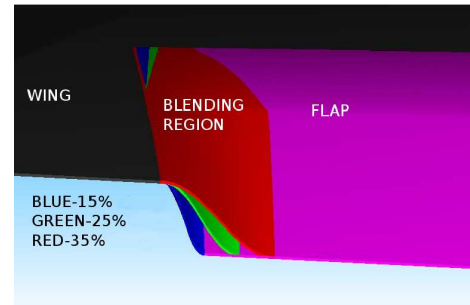


(d)  $\alpha=15^\circ$ .

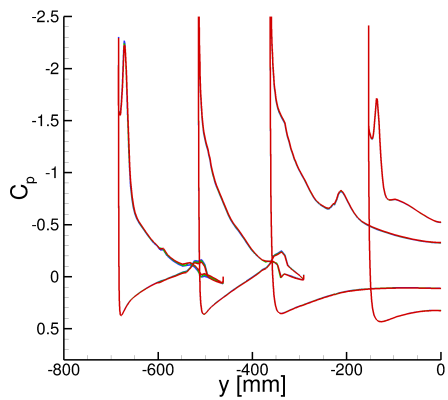
Fig. 7: Surface pressure comparison for block structured predictions and experiment at  $M=0.146$ . Flow visualisation is for  $C_p$  contours and skin friction streamlines. The labelling of slices is as indicated in Fig. 1.



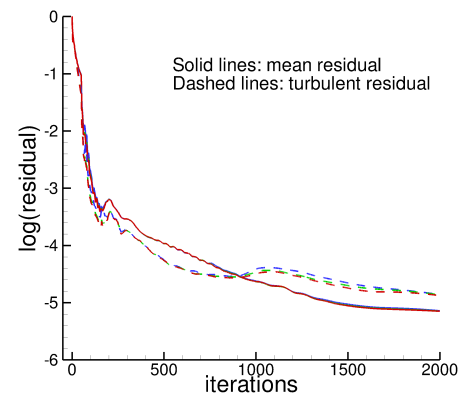
(a)  $\alpha=10^\circ$  .



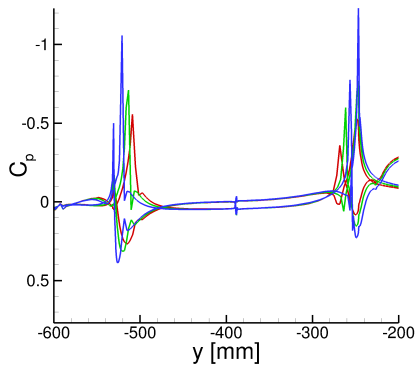
(b) Width of the different blendings.



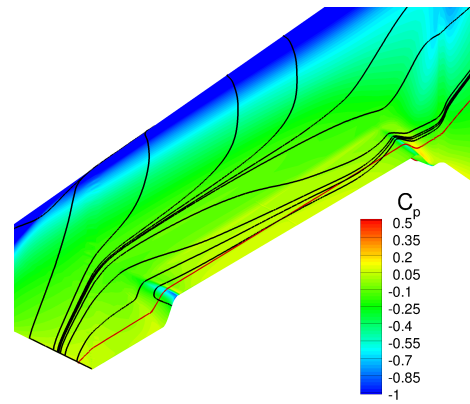
(c)  $\alpha=15^\circ$  .



(d)  $\alpha=15^\circ$  .

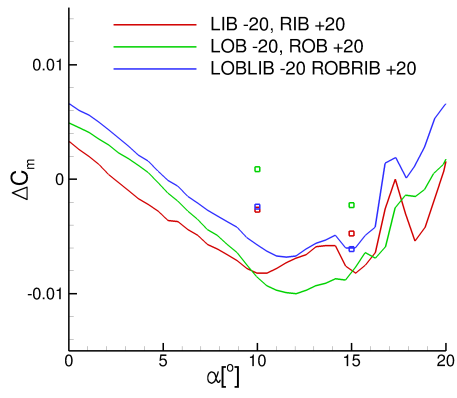


(e) Slice across the flap,  $\alpha=15^\circ$  .

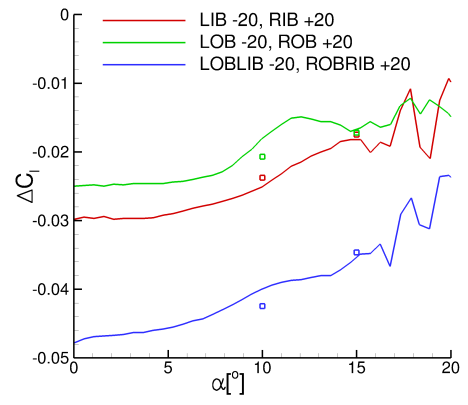


(f) Flow visualisation for the medium blending,  $\alpha=15^\circ$  , red line indicates where slice in (e) is.

Fig. 8: Comparison of block structured results using different blending widths for the LOB +20° LIB +20° configuration at  $M=0.146$ . The lines are coloured as in (b).

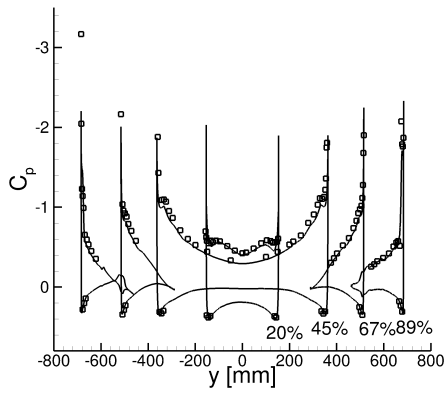


(a) Pitching moment coefficient.

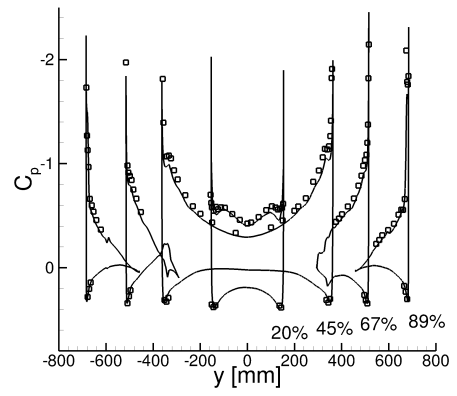


(b) Rolling moment coefficient.

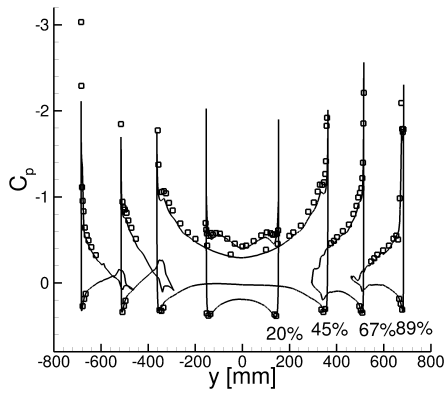
Fig. 9: Incremental forces for various flap deflections at  $M=0.146$ , block structured results. The lines and symbols correspond to the experiment and CFD, respectively.



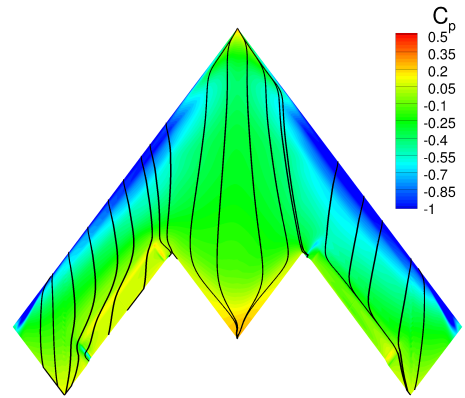
(a) LOB  $-20^\circ$ , ROB  $+20^\circ$ .



(b) LIB  $-20^\circ$ , RIB  $+20^\circ$ .

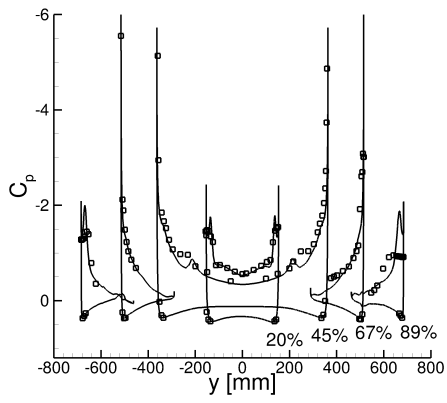


(c) LOBLIB  $-20^\circ$ , ROBRIB  $+20^\circ$ .

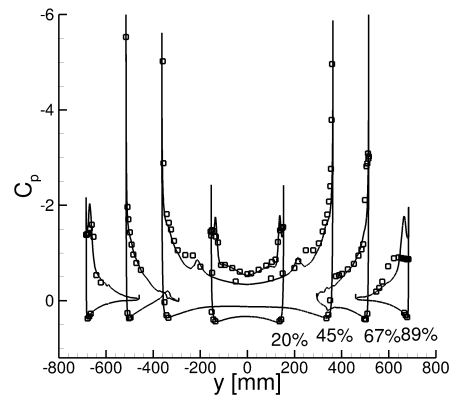


(d) LOBLIB  $-20^\circ$ , ROBRIB  $+20^\circ$ , flow visualisation.

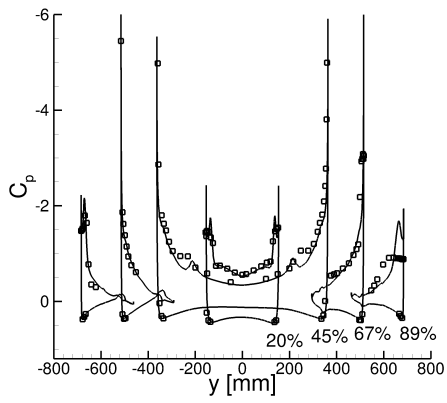
Fig. 10: Surface pressure comparison for block structured results at  $M=0.146$ ,  $\alpha=10^\circ$ . The lines and symbols correspond to the CFD and experiment, respectively, with skin friction streamlines added in part d.



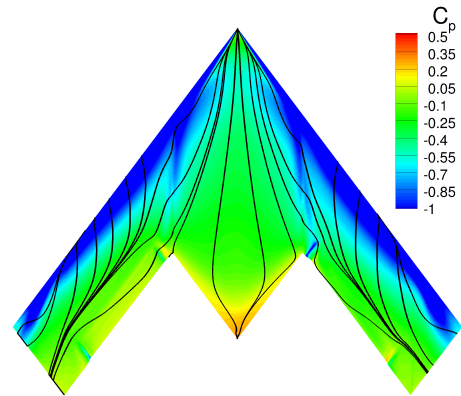
(a) LOB  $-20^\circ$ , ROB  $+20^\circ$ .



(b) LIB  $-20^\circ$ , RIB  $+20^\circ$ .

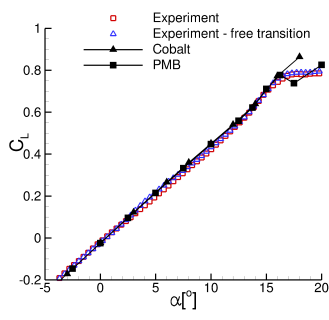


(c) LOBLIB  $-20^\circ$ , ROBRIB  $+20^\circ$ .

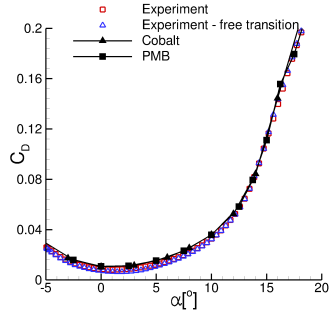


(d) LOBLIB  $-20^\circ$ , ROBRIB  $+20^\circ$ , flow visualisation.

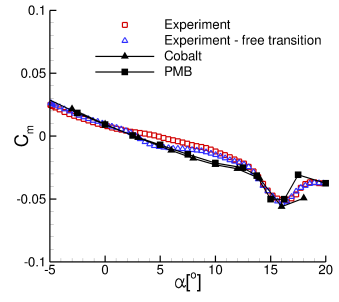
Fig. 11: Surface pressure comparison for block structured results at  $M=0.146$ ,  $\alpha=15^\circ$ . The lines and symbols correspond to the CFD and experiment, respectively, with skin friction streamlines added in part d.



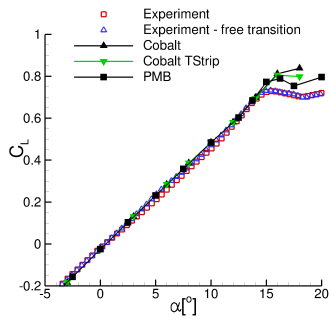
(a)  $M=0.5$ .



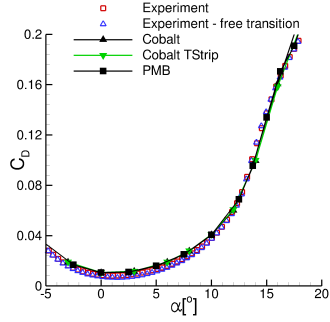
(b)  $M=0.5$ .



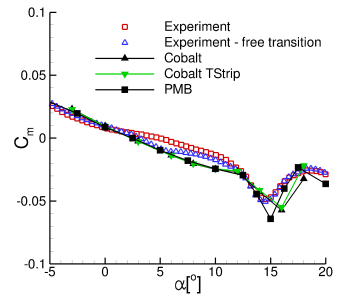
(c)  $M=0.5$ .



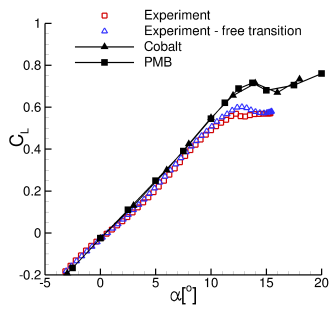
(d)  $M=0.7$ .



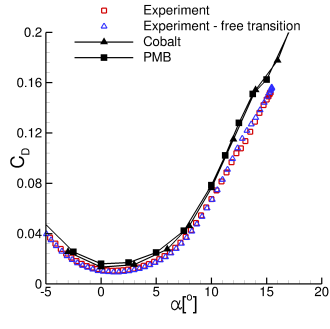
(e)  $M=0.7$ .



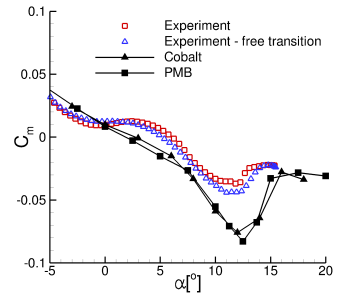
(f)  $M=0.7$ .



(g)  $M=0.9$ .



(h)  $M=0.9$ .



(i)  $M=0.9$ .

Fig. 12: Clean configuration forces and moments.

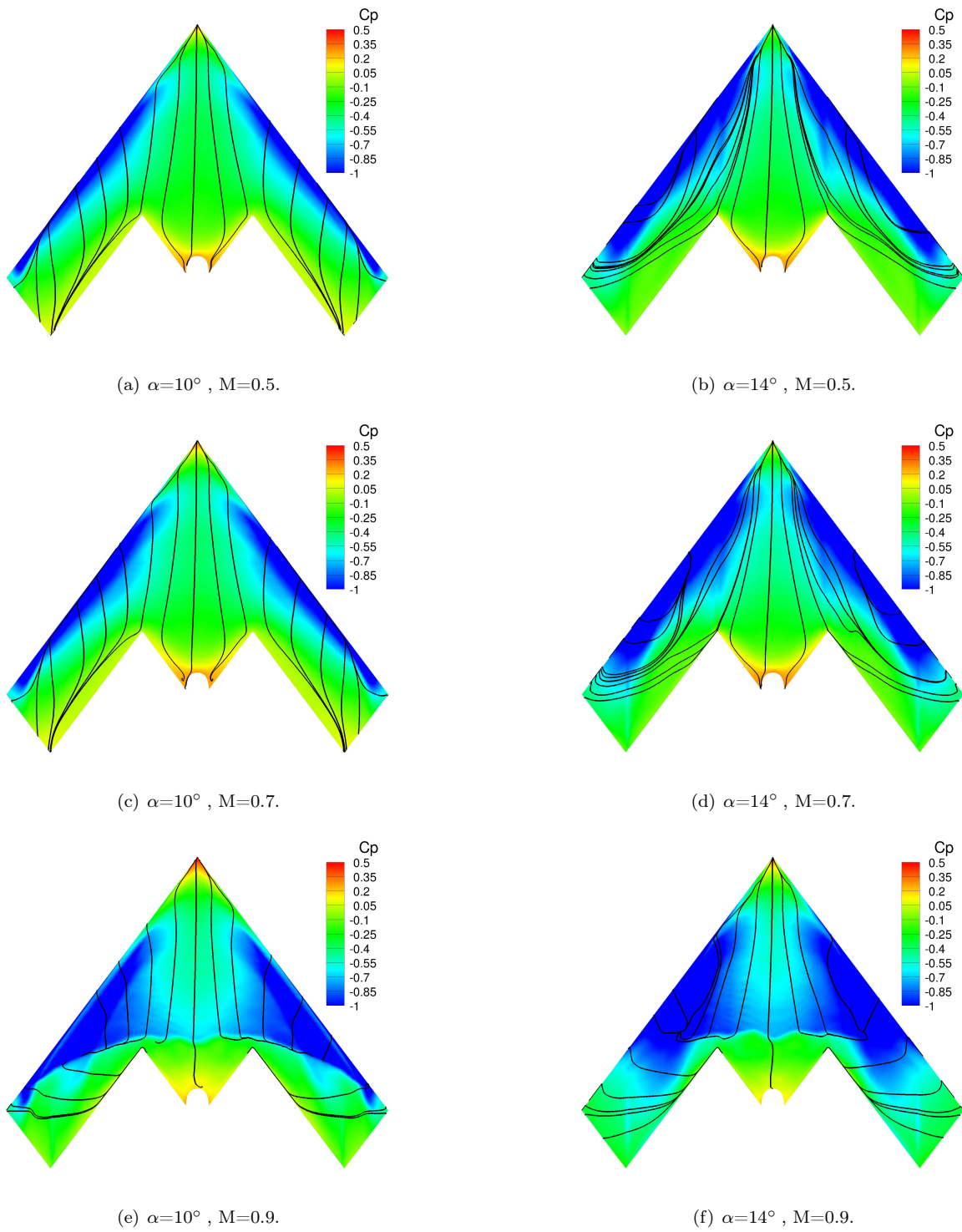


Fig. 13: Clean configuration flow visualisation for three Mach numbers, unstructured results. The two columns correspond to angles of attack of  $10^\circ$  and  $14^\circ$ , respectively.

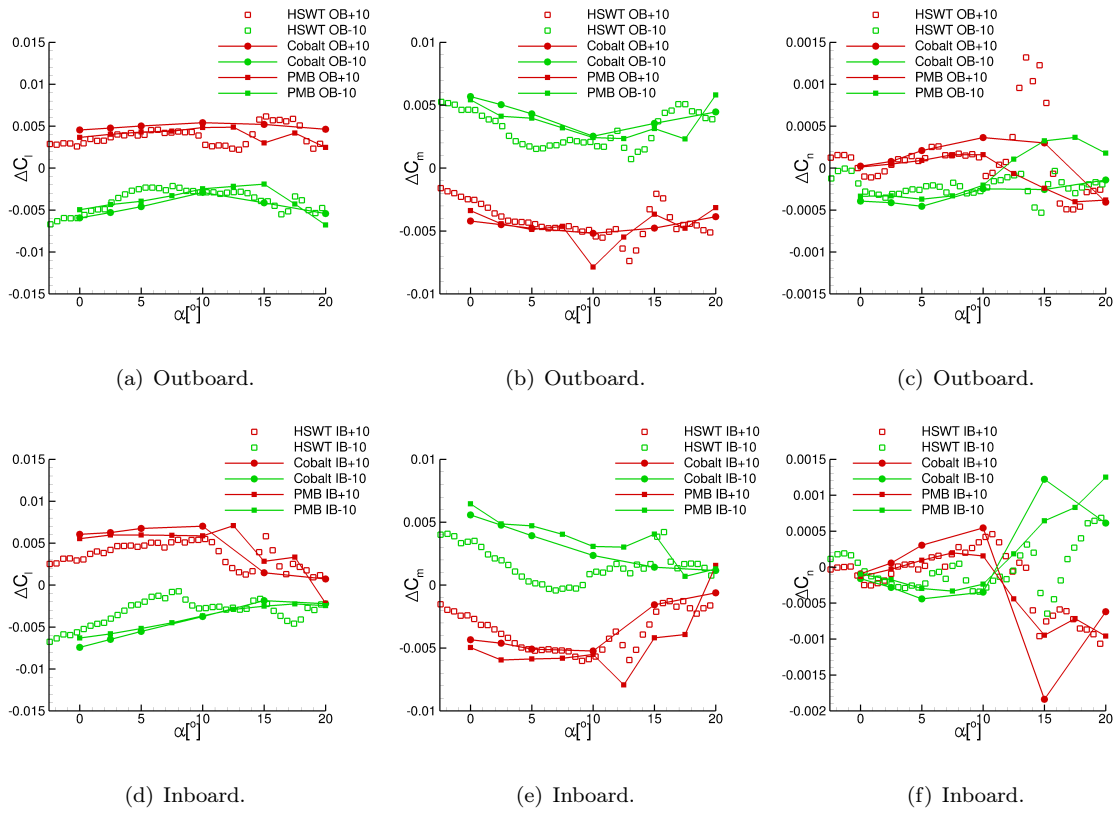


Fig. 14: Incremental forces for the outboard and inboard flaps deflected at  $\pm 10^\circ$  at  $M=0.7$ . The two rows correspond to the outboard and inboard flap deflections, respectively.

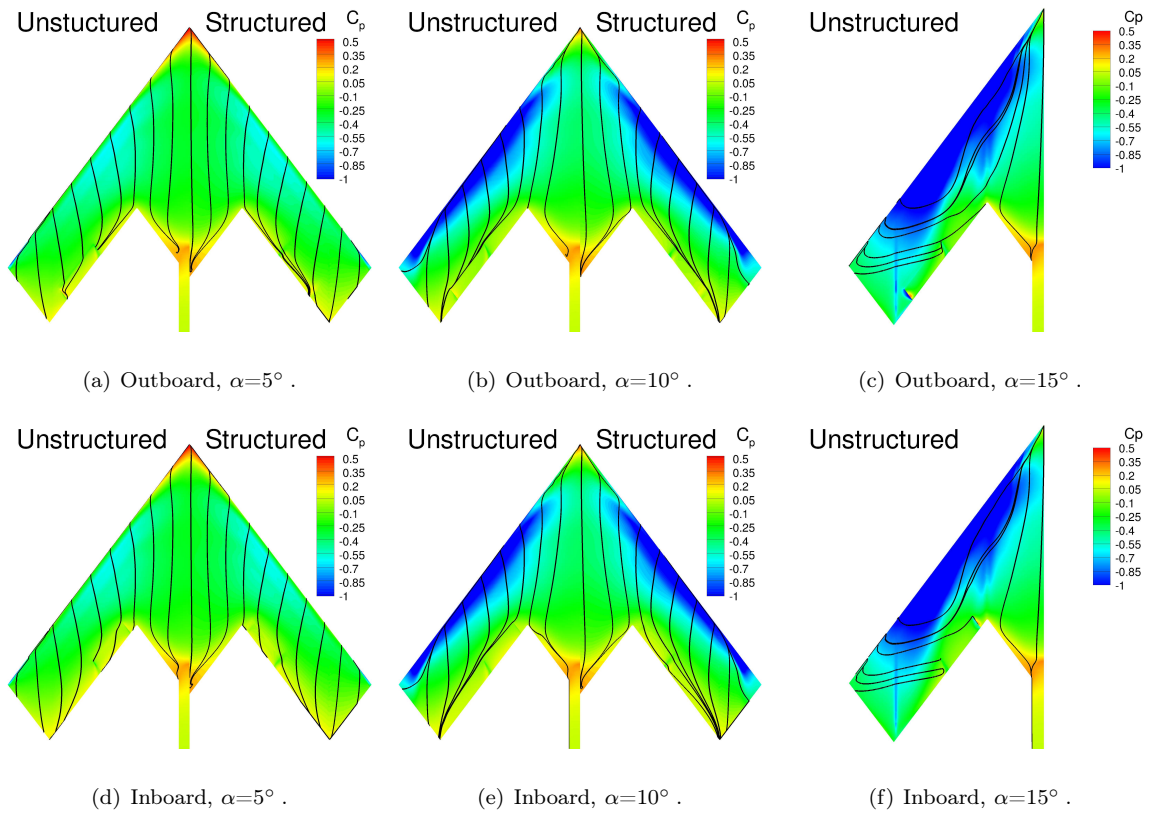
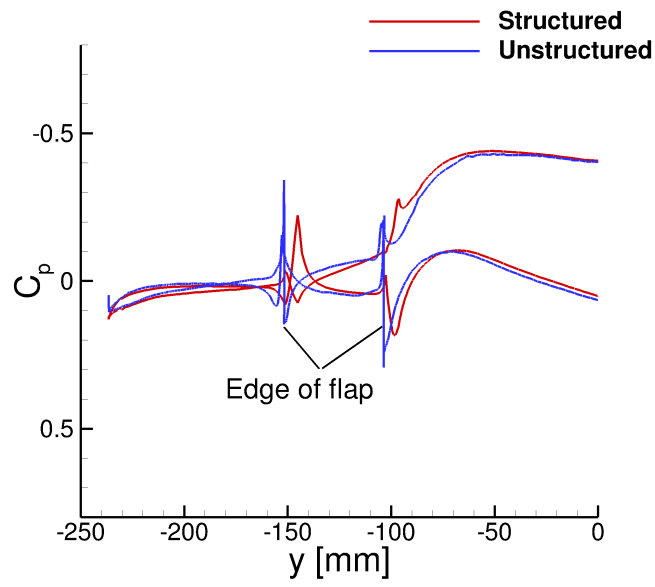
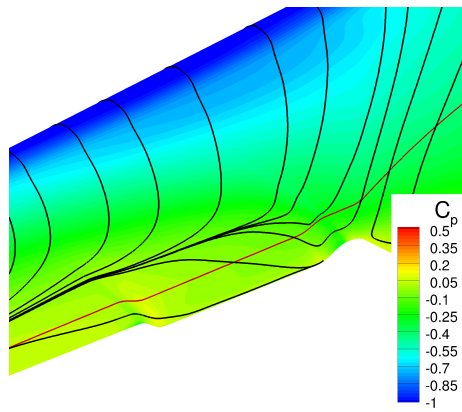


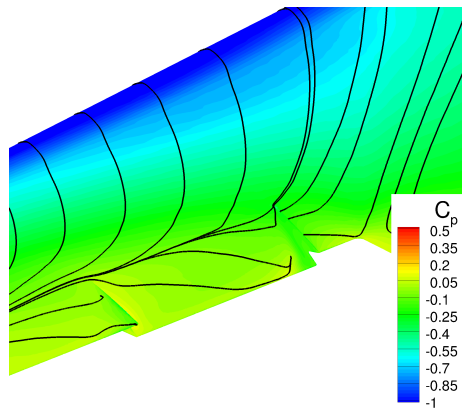
Fig. 15: Flow visualisation for the outboard and inboard flaps deflected at  $-10^\circ$  and  $+10^\circ$ , respectively, at  $M=0.7$ ,  $C_p$  and skin friction streamlines.



(a) Slice across the flap.

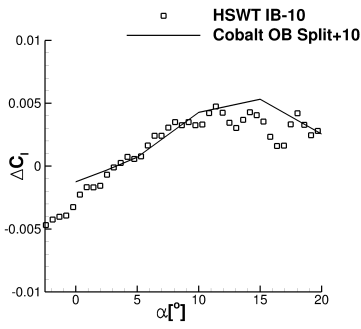


(b) Structured results.

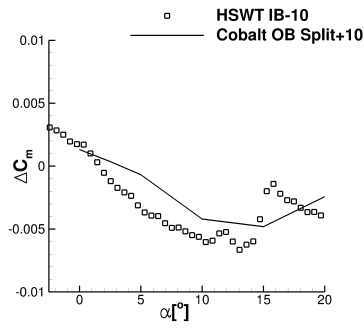


(c) Unstructured results.

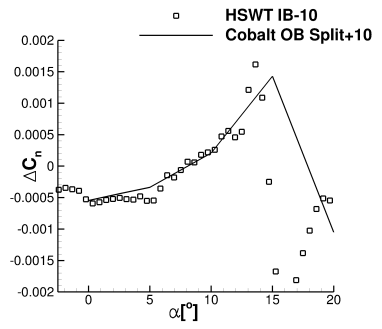
Fig. 16: Surface pressure comparison and flow visualisation for the structured and unstructured results at  $M=0.7$ ,  $\alpha=10^\circ$  for the inboard flap at  $10^\circ$ . The red line in (b) indicates where the slice in (a) was taken from.



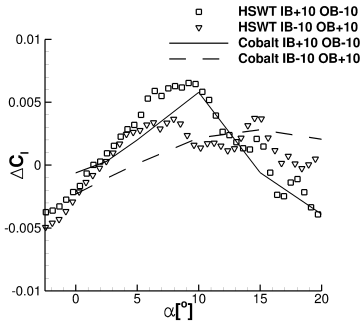
(a) Split.



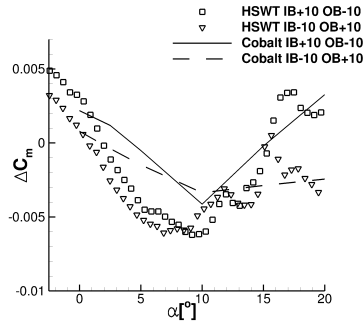
(b) Split.



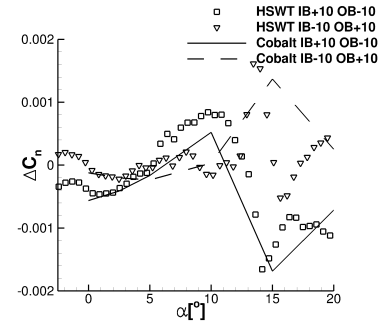
(c) Split.



(d) Crow.



(e) Crow.



(f) Crow.

Fig. 17: Incremental forces for the split flap and crow flaps at  $M=0.7$ .

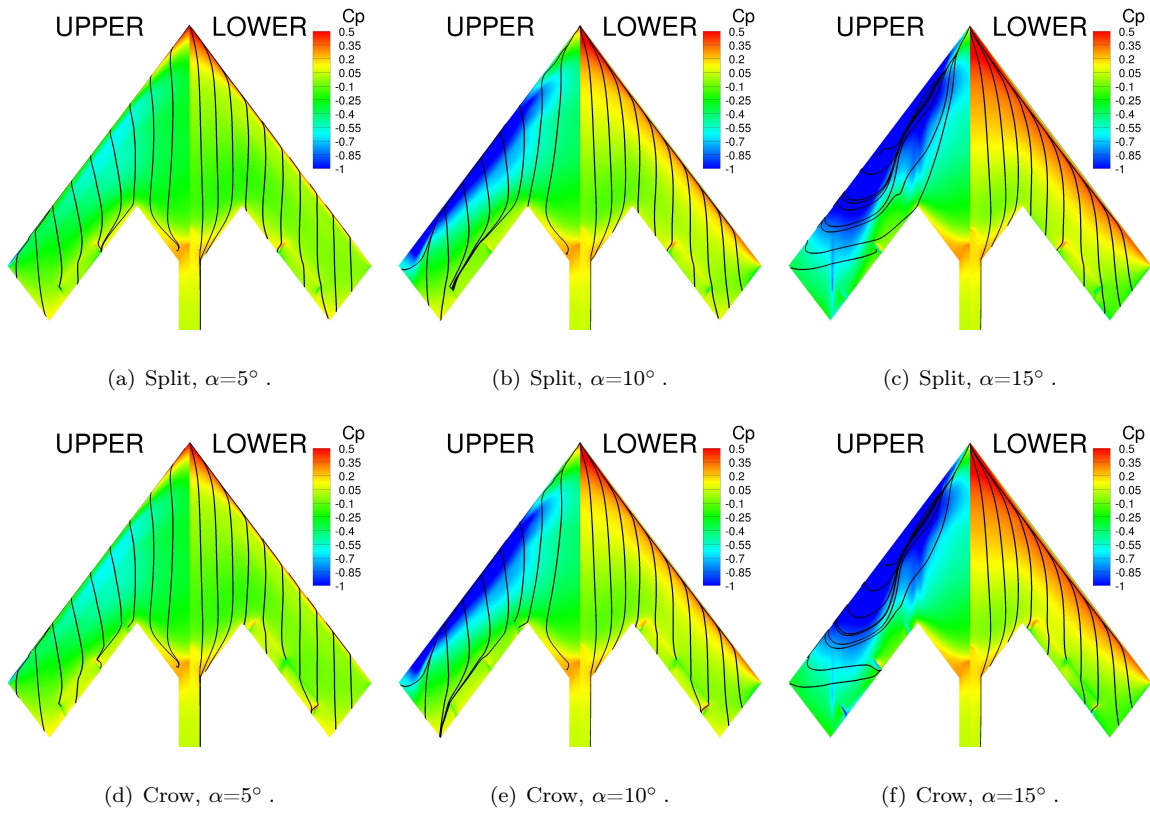


Fig. 18: Flow visualisation for the split flap and the crow flaps (OB -10, IB +10) deflected at  $M=0.7$ ,  $C_p$  and skin friction streamlines, unstructured results.